Photo-acoustic detection of chirality in metal-polystyrene metasurfaces

ⓘD E. Petronijević, G. Leahu, ⓘD R. Li Voti, et al.

View Online Export Citation CrossMark

ARTICLES YOU MAY BE INTERESTED IN

Large vacuum Rabi splitting between a single quantum dot and an H0 photonic crystal nanocavity
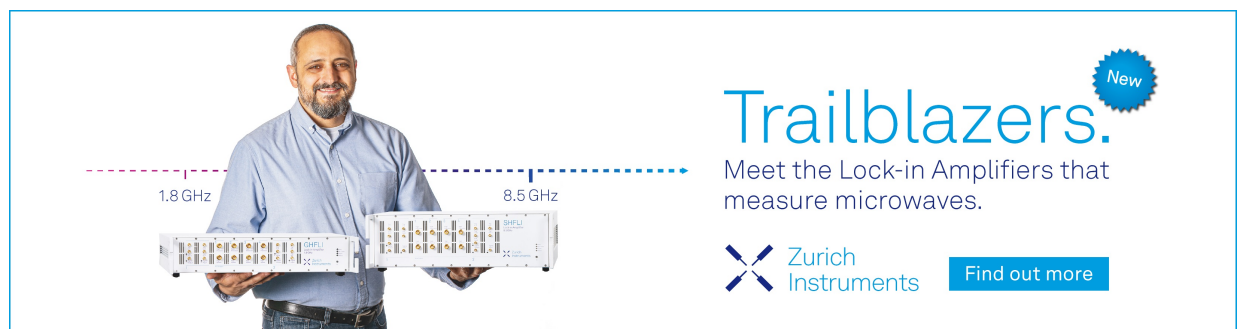Applied Physics Letters **112**, 093101 (2018); https://doi.org/10.1063/1.5016615

Ultrahigh refractive index sensitivity via lattice-induced meta-dipole modes in flat metallic nanoantenna arrays
Applied Physics Letters **112**, 223102 (2018); https://doi.org/10.1063/1.5031768

On-demand generation of background-free single photons from a solid-state source
Applied Physics Letters **112**, 093106 (2018); https://doi.org/10.1063/1.5020038

Photo-acoustic detection of chirality in metal-polystyrene metasurfaces

View Online　　Export Citation　　CrossMark

E. Petronijević,[1,a] G. Leahu,[1] R. Li Voti,[1] A. Belardini,[1] C. Scian,[2] N. Michieli,[2] T. Cesca,[2] G. Mattei,[2] and C. Sibilia[1]

AFFILIATIONS

[1] Department S.B.A.I., Sapienza Università di Roma, Via A. Scarpa 14, I-00161 Rome, Italy
[2] Physics and Astronomy Department, University of Padova, via Marzolo 8, I-35131 Padova, Italy

[a] Electronic mail: emilija.petronijevic@uniroma1.it

ABSTRACT

Nowadays, nanophotonics aims towards low-cost chip-scale devices that can tailor electromagnetic properties, one of which is the control of circular polarization at the nanoscale. Here, we demonstrate the chiral properties of metasurfaces produced by means of nanosphere lithography combined with tilted metal deposition. We apply the photo-acoustic technique to characterize the circular dichroism (CD) at 633 nm of polystyrene nanospheres covered by three different metals: Au- and Cr-covered samples show extrinsic chiral behavior, while the Ag-covered sample shows CD at normal incidence, characteristic of intrinsic chirality. As the experimental data are in good agreement with numerical predictions, we believe that such design can be optimized to get efficient circularly polarized detection at the nanoscale.

Published under license by AIP Publishing. https://doi.org/10.1063/1.5064514

Chirality, a lack of the mirror symmetry of an object,[1] is an important property of some of the building blocks of our world (many molecules, DNA, sugars, and drugs). Two mirror images of a chiral object differ only in spatial arrangement,[2] which leads to different interactions with circularly polarized light (CPL) of opposite handedness;[3] namely, optical activity (OA) and circular dichroism (CD) are the refractive index and the absorption difference, respectively. Specifically, chirality of molecules influences their biological activities;[4] e.g., only one mirror image of a chiral drug has desirable effects on the human body, while another can lead to serious side-effects.[5] As the chiral medium affects the absorption and/or phase velocity of CPL passing through it, OA and CD measurements are conventionally used to determine the molecules' chirality. However, most of the chiral molecules have extremely low CD (mdeg range), which complicates CD measurements due to high concentration and long integration time requirements.[6] Over the past few years, the nanoscale community has proposed especially designed chiral nanostructures[7,8] which exhibit CD behavior and are able to enhance the interaction with molecules, thus improving the chiral sensing.[9] When the nanostructures are comparable to or smaller than the light wavelength and organized periodically, they form a *metasurface*; generally, if the symmetry of the metasurface is broken, a chiral

behavior is expected.[10] Geometric features of intrinsically chiral metasurfaces (usually helix or gammadion-like) can be complicated to fabricate and implement at the nanoscale. This problem can be solved by a proper experimental set-up where the incident light wavevector, the average surface normal, and the sample direction must be nonplanar. Such chiral behavior is called *extrinsic* chirality, and it is governed by both the experimental set-up and the metasurface, which can be achiral itself.[11] Therefore, extrinsic chirality allows for the use of achiral nanostructures, which simplifies the nanofabrication, but provides CD only at oblique incidence.[11–16]

Here, we investigate the absorption properties of metasurfaces based on ordered polystyrene nanosphere (NS) monolayers, partially covered by metals (Au, Cr, or Ag). In such samples, the combination of geometrical parameters (such as the NS diameter and direction of metal deposition) and the type of metal lead to intriguing chiral behavior. We use photoacoustic spectroscopy to characterize different absorption for right and left circular polarization (RCP and LCP), giving CD as a direct result. Moreover, experimental results are in good agreement with numerical work.

Gold, chromium, and silver tilted semi-nanoshell arrays (SNSAs) were produced by nanosphere lithography (NSL) on soda-lime glass substrates,[17–19] as explained in detail in supplementary

material 1. 2D arrays of hexagonal unit cells with polystyrene (PS) nanospheres of diameter $D_p \sim 370$ nm were covered with a 50 nm thick metallic layer of Au, Cr, or Ag by thermal evaporation with a tilt angle of 45° with respect to the sample's surface; for Ag-SNSA, an additional in-plane tilt was introduced. Due to the non-closely packed nature of the 2D array, a metallic layer (in the following labelled as the metallic grid) was formed at the substrate surface following the geometric shadow of the PS nanospheres. As an example, in Figs. 1(a)–1(c), we report the FE-SEM images in plane view of the tilted Au-SNSA, Cr-SNSA, and Ag-SNSA samples, respectively, while a sketch of the samples is given in Fig. 1(d). For Ag-SNSA, a more regular and prominent metallic grid was formed on the substrate, which is tilted with respect to the hexagon axes, leading to a specific asymmetry of this sample, as it will be reported below.

First, we spectrally characterize the samples' absorption by means of the photo-acoustic (PA) technique;[15,20–23] the basic PA principles and the PA set-up details are given in supplementary material 2. First, in order to distinguish the contribution of the nanostructure to the PA signal, we measure the spectra of a reference sample, which is a flat metallic film deposited on the same substrate near the 2D array of polystyrene NS during the evaporation, and normalize the results to the absorption of graphite, obtaining the spectra reported in Fig. 2(a). In the UV region, they are all dominated by the soda-lime glass substrate absorption (below 300 nm). In the visible and near-infrared regions, the PA signal strongly decreases above the interband absorption threshold for Au and Ag, while for Cr, it decreases gradually; the soda-lime glass substrate shows negligible absorption. Next, we measure the PA spectra of SNSA arrays and normalize them to the zones without NS, Fig. 2(b). There is a clear absorption increase for Ag- and Au-SNSA above the interband threshold wavelength, while for Cr-SNSA, this ratio reaches 2. Such an increase can be attributed to the fact that a
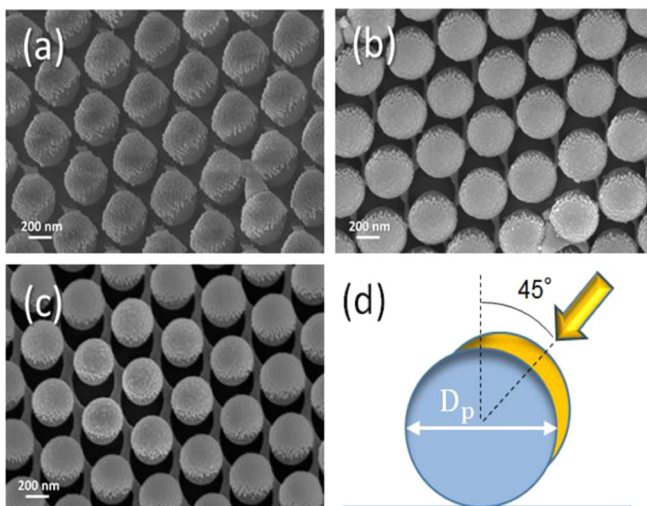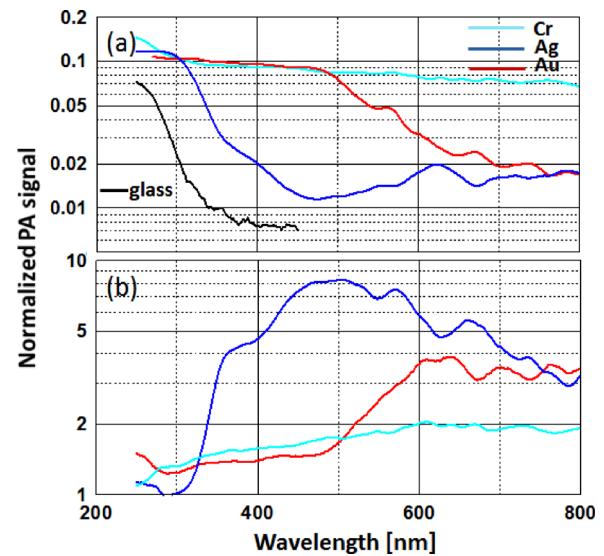

FIG. 2. (a) PA spectra of the soda-lime glass substrate (black) alone and covered with a thin layer of Au (red), Ag (blue), or Cr (cyan); the spectra are normalized to the PA signal of graphite. (b) PA signal of SNSAs normalized to the respective flat metal film from (a) for Au-SNSA (red), Ag-SNSA (blue), and Cr-SNSA (cyan).

continuous material dissipates heat better than a nanostructured one, especially if the nanostructure lies upon a scarce heat conductor such as polystyrene; this leads to a higher local temperature change for the SNSA and, finally, to a higher PA amplitude.

Since all three samples have a notable PA increase at 633 nm, we further chose this wavelength for CD characterization. We adapted the PA set-up for extrinsic chirality measurements, where we shine a 633 nm laser on the samples under an angle of incidence θ with respect to the sample normal $\vec{s}$. Since the metal deposition on top of the nanospheres is not symmetrical (thermal evaporation at 45°), with oblique incidence, these structures are expected to exhibit extrinsic chirality when the incidence wavevector $\vec{k}$, the average surface normal to the metallic nanocrescents $\vec{n}$, and the sample normal $\vec{s}$ are out of plane.[11,16,24] A sketch of such an experimental configuration is shown in Fig. S3(a): the substrate normal $\vec{s}$ lies parallel to the z-axis, while the average surface normal $\vec{n}$ is given by the evaporation direction. For Au- and Cr-SNSA, $\vec{n}$ and $\vec{s}$ lie in the yz-plane and form an angle of 45° [Fig. S3(b)], while $\vec{k}$ and $\vec{s}$ lie in the xz-plane and form an angle θ; the top view sketch of the structure is shown in Fig. S3(c). For Ag-SNSA, the projection of $\vec{n}$ on the xy-plane forms an angle φ with respect to the y-axis [Fig. S4(b)]. Therefore, the PA set-up is set to scan over polarization and incidence angles [Fig. 3(a)]. The laser light is linearly polarized before the quarter wave plate, so that it can be **s**- or **p**-polarized with respect to the metal flux direction when the wave plate's fast axis is at 0°, inset of Fig. 3(a); this axis then scans the angles from −180° to 180°, where −45° represents RCP and +45° represents LCP. The PA cell is mounted on a rotating stage, enabling the incidence angle scan from $\theta = -50°$ to 50°. In Fig. 3(b), we show the PA signal dependence on the quarter waveplate

FIG. 1. Plane view FE-SEM images of the tilted (a) Au-SNSA, (b) Cr-SNSA, and (c) Ag-SNSA and (d) sketch of the geometric parameters and the evaporation angle.
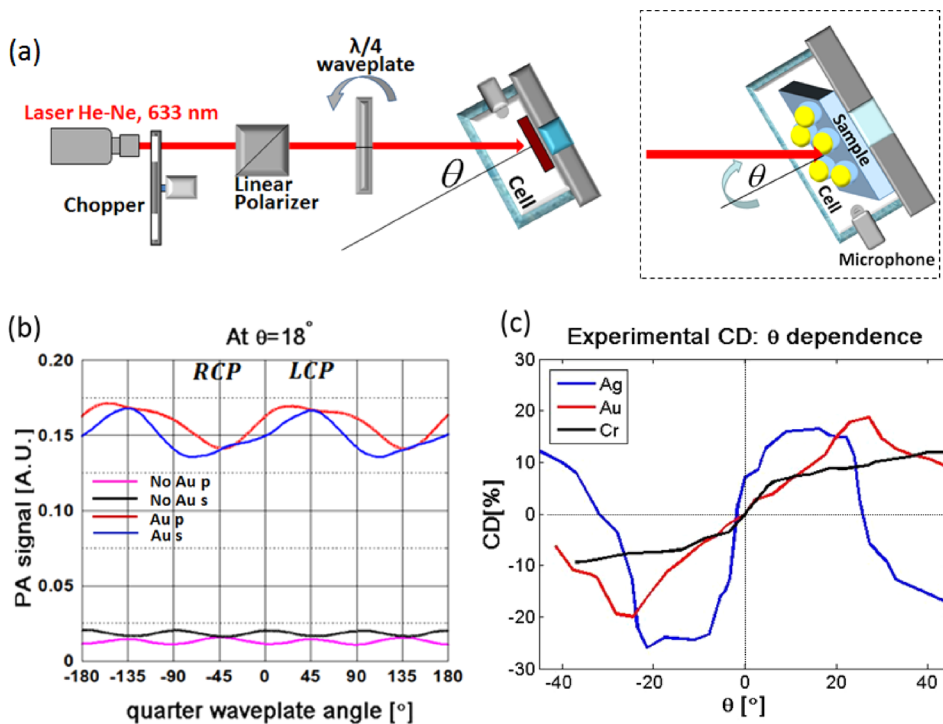
FIG. 3. (a) PA set-up for the chiral characterization: the He-Ne laser is followed by a chopper and a linear polarizer, after which a quarter waveplate defines circular polarization. Inset: Sample with a metallic cap under oblique incidence. (b) Quarter waveplate polarization scan at $\theta = 18°$ of incidence, for PS nanospheres before and after the Au deposition. (c) CD dependence on the angle of incidence for the three samples.

rotation at $\theta = 18°$ for Au-SNSA; for comparison, we show the results obtained for the same sample before the Au evaporation. As expected, the structure without metal is completely symmetric and shows no difference for LCP and RCP absorption, while we note a different response at $\pm 45°$ rotation when it is covered with Au. This is a typical behavior for extrinsically chiral nanostructures, which possess CD at oblique incidence. We further introduce a figure of merit for CD in the PA measurements as

$$CD[\%] = \frac{A_{LCP} - A_{RCP}}{A_{LCP} + A_{RCP}} \cdot 200, \qquad (1)$$

where A_{LCP} and A_{RCP} are the PA signal amplitudes for the quarter waveplate rotation of $+45°$ and $-45°$, respectively. In Fig. 3(c), we show the measured CD as a function of the incident angle for the three samples. We see that for the Au- and Cr-SNSA, CD increases from 0% at normal incidence for positive angles of incidence and becomes negative for negative angles, inverting its sign (typical for extrinsic chirality). The maximum CD is reached for Au-SNSA (CD of around 18%) at $\theta \approx 25°$, while a different behavior is observed for Cr-SNSA, which in this wavelength range has the maximum absorption, and hence, its geometric parameters play a minor role in CD. The most interesting is the Ag-SNSA whose CD varies rapidly from $\theta = -10°$ to $\theta = 10°$, while at normal incidence, this sample provides nonzero CD ($\approx 7\%$), which is a property of intrinsically chiral structures.[25] Moreover, the overall absorption has a much higher contribution of the Ag grid on the substrate surface, formed due to the NS shadow during the evaporation, as it was recently reported in the plasmonic metasurfaces fabricated by a similar procedure.[19,26–30] However, here, the peculiar behavior of

Ag-SNSA arises due to the nanocrescents and grids rotated with respect to the hexagonal symmetry: if the xy-plane projection of the flux direction $\vec{n}_{xy}$ lies parallel to one of the hexagonal symmetry directions, only extrinsic chirality can be observed under oblique angles, Fig. S4(a); otherwise, the offset angle between these directions makes the metallic grid and nanocrescents asymmetric even at the normal incidence, Fig. S4(b).

It is worth noting that the dramatic differences in CD behavior cannot be attributed only to the different optical constants of the metals. Here, we point out that the initial fabrication parameters, except for the in-plane tilt in Ag-SNSA, were equal (this tilt only introduces a CD shift from the extrinsic one), while the final nanostructures obviously differ in terms of the metallic part attached on the nanosphere and the grid on the substrate [Figs. 1(a)–1(c)]. Therefore, there is a high contribution of the morphological differences in the finalized samples; as Cr attaches well to the polystyrene, the mostly regular semishells and a rather small contribution of the grid are present in Cr-SNSA, while in Au-SNSA, semishells slightly deviate from the spherical shape and there is no real grid formed. Finally, Ag-SNSA, apart from the semishell, has a distinguishable elliptical nanohole array formed on the substrate, which we attribute to the lower material stability to attach on the nanosphere during the tilted evaporation. Rendering these properties perfectly controllable is a subject of the current work. In order to gain insights into the nanoscale absorption distribution, we modelled SNSA electromagnetic behavior in Lumerical;[31] the nanoshell dimensions and the metallic grid contribution were estimated from SEM images (the details are given in supplementary material 3). In Fig. 4(a), the calculated CD is in very good agreement
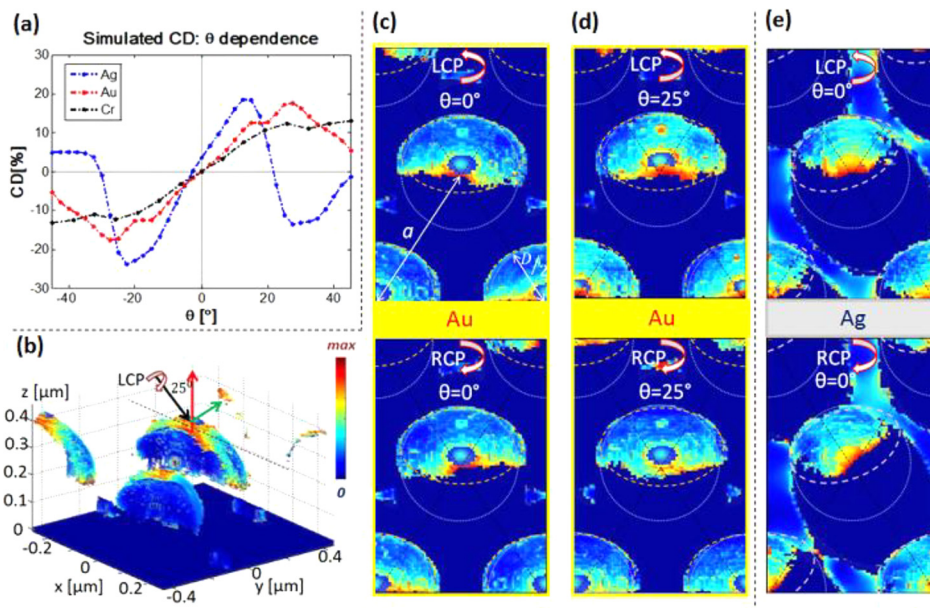
FIG. 4. (a) Calculated CD dependence on the angle of incidence. (b) 3D distribution of the absorption density in a unit cell of Au-SNSA at $\theta = 25°$ and LCP (maximum CD). Top views (xy plane) of the absorption maps shown in Figs. S5 and S6 for opposite handedness for (c) Au-SNSA at $\theta = 0°$, (d) Au-SNSA at $\theta = 25°$, and (e) Ag-SNSA at $\theta = 0°$.

with the PA results in terms of both shape and absolute values. Next, in Fig. 4(b), we show the absorption density calculated over the unit cell volume for the condition of maximum CD for Au-SNSA at 25°. As expected, the maximum absorption density is on the borders of the Au nanocrescent and controls the whole response of the metallic nanostructure; the grid on the substrate has a negligible influence, and the absorption distribution at normal incidence is antisymmetric with respect to the y-axis and equal when integrated over space for LCP and RCP (see the 3D map in Fig. S6). In Figs. 4(c)–4(e), for the sake of clarity, we show the xy top view of the absorption maps. For Au-SNSA, at normal incidence, the antisymmetry of the distribution in Fig. 4(c) is in agreement with extrinsic chirality; consistently, at $\theta \approx 25°$, LCP is more absorbed than RCP, Fig. 4(d). In Fig. 4(e), we investigate Ag-SNSA at normal incidence: here, LCP is more absorbed, thus providing the positive non-zero CD due to the offset with respect to the hexagonal symmetry; as both the grid and the nanocrescents above the PS nanospheres are tilted providing the chiral behavior, at $\theta \approx 25°$, they cancel out, thus leading to CD $= 0$ [from the integration of the absorption in Fig. S7(b)]. Finally, the removal of the nanospheres could lead to even higher CD of the grid which is made of elliptical nanoholes, as shown in CD simulation of the Ag nanogrid only in Fig. S8. This could make the NSL technique of great interest for the chiral properties of surface plasmon polaritons,[32] as it offers many degrees of freedom (periodicity, ellipse parameters, metal type, thickness, etc.).

In conclusion, in this work, we have presented the CD behavior of metasurfaces consisting of polystyrene nanospheres asymmetrically covered with Au, Ag, or Cr. SNSAs were realized by NSL on soda-lime glass substrates and tilted evaporation of the metals. An extrinsic chiral response is detected as a CD dependence on the input beam angle of incidence. The maximum CD is observed at 25° for Au-SNSA, the least pronounced CD is found for Cr, while the Ag-SNSA also provides CD at normal incidence, due to the tilted deposition with respect to the hexagonal symmetry. The numerical calculations closely follow PA results and reveal that these samples tailor CD by controlling the absorption distribution. Therefore, we propose NSL along with the tilted metal evaporation for the fabrication of chiral nanodevices, whose chiral behavior can be characterized by the scattering-free, stable, and simple PA technique. We believe that such an approach can lead to applications in chiral sensing and chiral light manipulation at the nanoscale.

See supplementary material which is divided into four sections. In supplementary material 1, we describe in more detail the fabrication of SNSAs based on nanosphere lithography and subsequent tilted thermal evaporation of the metallic layers. In supplementary material 2, we explain the basic physics behind the PA technique and give details of the PA set-up used for the experiments. In supplementary material 3, we present numerical work done in order to investigate the absorption of SNSAs at the nanoscale. Finally, in supplementary material 4, all supplementary figures are given.

REFERENCES

[1]L. Kelvin, *The Molecular Tactics of a Crystal* (Clarendon Press, Oxford, 1894).

[2]L. A. Nguyen, H. He, and C. Pham-Huy, Int. J. Biomed. Sci. **2**(2), 85–100 (2006).

[3]A. Rodger and B. Nordén, *Circular Dichroism and Linear Dichroism* (Oxford University Press, Oxford, 1997).

[4]A. J. Hutt and S. C. Tan, Drugs **52**, 1–12 (1996).

[5]S. K. Teo, W. A. Colburn, W. Tracewell, K. Kook, D. Stirling, M. Jaworsky, M. Scheffler, S. Thomas, and O. Laskin, Clin. Pharmacokinet. **43**, 311–327 (2004).

[6]S. M. Kelly, T. J. Jess, and N. C. Price, Biochim. Biophys. Acta **1751**, 119–139 (2005).

[7]V. K. Valev, J. J. Baumberg, C. Sibilia, and T. Verbiest, Adv. Mater. **25**(18), 2517–2534 (2013).

[8]X.-T. Kong, L. V. Besteiro, Z. Wang, and A. O. Govorov, "Plasmonic chirality and circular dichroism in bioassembled and nonbiological systems: Theoretical background and recent progress," Adv. Mater. (published online).

[9]Y. Zhao, A. N. Askarpour, L. Sun, J. Shi, X. Li, and A. Alù, Nat. Commun. **8**, 14180 (2017).

[10]T. Verbiest, M. Kauranen, A. Persoons, M. Ikonen, J. Kurkela, and H. Lemmetyinen, J. Am. Chem. Soc. **116**, 9203 (1994).

[11]E. Plum, X.-X. Liu, V. A. Fedotov, Y. Chen, D. P. Tsai, and N. I. Zheludev, Phys. Rev. Lett. **102**, 113902 (2009).

[12]A. Belardini, M. Centini, G. Leahu, D. C. Hooper, R. Li Voti, E. Fazio, J. W. Haus, A. Sarangan, V. K. Valev, and C. Sibilia, Sci. Rep. **6**, 31796 (2016).

[13]I. De Leon, M. J. Horton, S. A. Schulz, J. Upham, P. Banzer, and R. W. Boyd, Sci. Rep. **5**, 13034 (2015).

[14]T. Cao, C. Wei, L. Mao, and Y. Li, Sci. Rep. **4**, 7442 (2014).

[15]G. Leahu, E. Petronijevic, A. Belardini, M. Centini, C. Sibilia, T. Hakkarainen, E. Koivusalo, M. Rizzo Piton, S. Suomalainen, and M. Guina, Adv. Opt. Mater. **5**, 1601063 (2017).

[16]E. Petronijevic, M. Centini, A. Belardini, G. Leahu, T. Hakkarainen, and C. Sibilia, Opt. Express **25**(13), 14148–14157 (2017).

[17]T. Cesca, N. Michieli, B. Kalinic, I. G. Balasa, R. Rangel-Rojo, J. A. Reyes Esqueda, and G. Mattei, Mater. Sci. Semicond. Process. **92**, 2–9 (2019).

[18]V. Russo, N. Michieli, T. Cesca, C. Scian, D. Silvestri, M. Morpurgo, and G. Mattei, Nanoscale **9**, 10117 (2017).

[19]T. Cesca, N. Michieli, B. Kalinic, A. Sanchez-Espinoza, M. Rattin, V. Russo, V. Mattarello, C. Scian, P. Mazzoldi, and G. Mattei, Nanoscale **7**, 12411–12418 (2015).

[20]G. Leahu, E. Petronijevic, A. Belardini, M. Centini, R. Li Voti, T. Hakkarainen, E. Koivusalo, M. Guina, and C. Sibilia, Sci. Rep. **7**, 2833 (2017).

[21]E. Petronijevic, G. Leahu, V. Mussi, C. Sibilia, and F. A. Bovino, AIP Adv. **7**, 025210 (2017).

[22]E. Petronijevic, G. Leahu, A. Belardini, M. Centini, R. Li Voti, T. Hakkarainen, E. Koivusalo, M. Rizzo Piton, S. Suomalainen, M. Guina, and C. Sibilia, Int. J. Thermophys. **39**(3), 45 (2018).

[23]E. Petronijevic, G. Leahu, A. Belardini, M. Centini, R. Li Voti, T. Hakkarainen, E. Koivusalo, M. Rizzo Piton, S. Suomalainen, M. Guina, and C. Sibilia, Int. J. Thermophys. **39**(4), 46 (2018).

[24]A. Belardini, M. C. Larciprete, M. Centini, E. Fazio, C. Sibilia, D. Chiappe, C. Martella, A. Toma, M. Giordano, and F. Buatier de Mongeot, Phys. Rev. Lett. **107**, 257401 (2011).

[25]A. Belardini, A. Benedetti, M. Centini, G. Leahu, F. Mura, S. Sennato, C. Sibilia, V. Robbiano, M. C. Giordano, C. Martella, D. Comoretto, and F. Buatier de Mongeot, Adv. Opt. Mater. **2**, 208–213 (2014).

[26]H. Sánchez-Esquivel, K. Y. Raygoza-Sánchez, R. Rangel-Rojo, E. Gemo, N. Michieli, B. Kalinic, J. A. Reyes-Esqueda, T. Cesca, and G. Mattei, Sci. Rep. **7**, 5307 (2017).

[27]Z. Li, E. Rusli, C. Lu, A. Bimo Prakoso, M. Foldyna, R. Khoury, P. Bulkin, J. Wang, W. Chen, E. Johnson, and P. Cabarrocas Caoa, Nanomaterials **8**(8), 626 (2018).

[28]A. Benedetti, A. Belardini, A. Veroli, M. Centini, and C. Sibilia, J. Appl. Phys. **116**, 164312 (2014).

[29]V. E. Bochenkov and D. S. Sutherland, Opt. Express **26**(21), 27101–27108 (2018).

[30]Y. Wang, J. Qi, C. Pan, Q. Wu, J. Yao, Z. Chen, J. Chen, Y. Li, X. Yu, Q. Sun, and J. Xu, Sci. Rep. **8**, 3351 (2018).

[31]See http://www.lumerical.com/tcad-products/fdtd/ for "Lumerical Solutions, Inc."

[32]T. Cao and M. J. Cryan, J. Electromagn. Wave Appl. **26**(10), 1275–1282 (2012).